Journal of Thermal Science Vol.32, No.2 (2023) 753−769

https://doi.org/10.1007/s11630-022-1744-0 **Article ID: 1003-2169(2023)02-0753-17**

A Confined Laminar Slot Impinging Jet at Low Reynolds Numbers: Unsteady Flow and Heat Transfer Characteristics

SHI Lei, SUN Chong, ZHU Xiaocheng*, DU Zhaohui

School of Mechanical Engineering, Shanghai Jiao Tong University, Shanghai 200240, China

Abstract: In this study, the unsteady flow and heat transfer characteristics of a laminar slot jet at low Reynolds numbers impinging on an isothermal plate surface in a two-dimensional confined space are numerically investigated. The investigations are performed at Reynolds numbers of 120, 150 and 200 based on the nozzle width and mean inlet velocity of the jet. Results show that the Reynolds numbers of 120, 150 and 200 correspond to different flow features, namely, a steady flow, an intermittent flapping motion of jet column and a continuous sinusoidal flapping state, respectively. Based on some time snapshots of the flow field, the dynamic characteristics and driving mechanism of the intermittent flapping motion of the jet column and the continuous sinusoidal flapping state are explained. When the jet flaps at the Reynolds number 150 and 200, there are other Nusselt number peaks outside the stagnation zone, which are related to the interference between the vortices shedding on both sides of the jet and the boundary layers of the plate surface. Furthermore, the dynamic mode decomposition is implemented to accurately extract flow modes with characteristic frequencies. For a Reynolds number of 150, there is a flapping mode, which describes the lateral flapping motion of the jet column. When the Reynolds number is 200, there are multiple modes related to the flapping motion of the jet, as well as a low-frequency mode, which reflects the periodic changes of the boundary contour and position of the recirculation zone.

Keywords: laminar slot impinging jet, unsteady flow, heat transfer, Nusselt number, dynamic mode decomposition

1. Introduction

Impinging jets have been broadly used to enhance the heat transfer in various industrial applications due to the high local heat transfer rates, such as turbine blade cooling [1], cooling of electronic equipment [2], drying of paper [3], food processing [4], or flow control of micro-electro-mechanical systems (MEMS) [5]. In some occasions, electronics components with micro-scale circuit components are cooled by the laminar impinging slot jets at low Reynolds numbers. However, to achieve a good heat transfer augmentation effect in these applications requires a clear understanding of the flow features of the laminar impinging slot jets at low Reynolds numbers, including the unsteady oscillatory behavior of the jets column, the interference between the vortex structures and the boundary layers after the jets impact the target surface, and the development of the vortex structures in the channel.

There have been many comprehensive reviews [6, 7] on the flow and heat transfer characteristics of the steady laminar jet impinging a target surface in the planar and

Received: Aug 15, 2021 AE: KAN Xiaoxu Corresponding author: ZHU Xiaocheng E-mail: zhxc@sjtu.edu.cn

Nomenclature

c_p	specific heat at constant pressure/J·(kg·K)$^{-1}$	$\boldsymbol{u}$	dimensionless velocity vector, scaled with U
e	height ratio, $e=H/W$	u_x	dimensionless transverse velocity component, scaled with U
f	frequency/s^{-1}	u_y	dimensionless streamwise velocity component, scaled with U
H	nozzle-plate spacing/m	W	jet nozzle width/m
h	convective heat transfer coefficient/ W·(m^2·K)$^{-1}$	x	dimensionless transverse coordinates, scaled with W
k	thermal conductivity/W·(m·K)$^{-1}$	y	dimensionless axial coordinates, scaled with W
L	channel length/m	θ	dimensionless temperature, $\theta=\dfrac{\hat{T}-T_0}{T_w-T_0}$
Nu	Nusselt number at the impingement surface, $Nu=hW/k$	μ	dynamic viscosity/Pa·s
$\overline{Nu}$	time-averaged Nusselt number at the impingement surface	ρ	density/kg·m^{-3}
p	dimensionless pressure, scaled with ρU^2	ω_z	z component of dimensionless vorticity vector, scaled with U/W
Pr	Prandtl number, $Pr=c_p\mu/k$	^	dimensional variable
Re	Reynolds number, $Re=\rho UW/\mu$	*	conjugate transpose
St_H	Strouhal number, $St_H=fH/U$		
T_0	inlet temperature of the jet/K	**Abbreviations**	
T_w	temperature of the impinging surface/K	DMD	dynamic mode decomposition
t	dimensionless time, scaled with W/U	FFT	fast Fourier transform
U	mean inlet velocity of the jet/m·s^{-1}	POD	proper orthogonal decomposition

the axisymmetric configurations. However, the laminar jet with such a geometric configuration can exhibit relatively novel unsteady flow characteristics, especially the unsteady oscillation behavior of the jet column. In the early days, Chiriac [8] numerically studied the flow and heat transfer features of a confined slot jet impinging on an isothermal plate and the Reynolds number ranging from 250 to 750. The results illustrated that the critical Reynolds number for the flow from steady state to unsteady state is between 585 and 610. When the Reynolds number is 750 (exceeding the critical Reynolds number), a low-frequency "flapping" instability of the jet occurs. Similarly, Lee et al. [9] numerically investigated the influence of the channel height on the unsteady flow and heat transfer characteristics of a laminar impinging slot jet, with the Reynolds number ranging from 50 to 500 and the height ratio (the ratio of channel height H to nozzle width W) from 2 to 5. The results show that the critical Reynolds number for the flow and temperature fields from steady state to unsteady state depends on the Reynolds number and height ratio, and when the flow is unsteady, as the Reynolds number increases, the jet flapping motion becomes more significant. The effect of Reynolds number (Re=100–1000) and channel height (H/W=2–10) on the unsteady oscillation behavior has been experimentally studied by Varieras et al. [10] using flow visualization technology. Their experiments revealed that the jet intensively sweeps the flat plate due to the self-oscillating bifurcation flow, and vortex dipoles generated near the plate surface are emitted alternately to both sides of the jet column.

In some investigations of laminar flow at low Reynolds numbers, various interesting flow bifurcation phenomena have been discovered. Uzol et al. [11] performed particle image velocimetry (PIV) measurements and numerical simulations to investigate the flow bifurcation of the jet impinging upon the concave wall. Results showed that for a jet exit Reynolds number of 321, the jet oscillation has obvious periodicity. Similarly, Lee et al. [12] employed flow visualization technique to investigate the flow characteristics of a micro-scale laminar jet at low Reynolds numbers (Re= 0.2–5.4) impacting the V-shaped plate. In the experiment, the periodic flapping motion of the jet was also observed, and it was found that even in micro-scale geometric configuration, the frequency of the jet flapping motion is linearly proportional to the flow velocity. Durst et al. [13] carried out a combined experimental and computational study of the symmetry-breaking bifurcation of the flow through a two-dimensional symmetrical sudden duct, with the channel Reynolds numbers of 70, 300, and 610, respectively. The results illustrated that when the channel

Reynolds number exceeds 125, a long and a short separation zones are formed in the channel due to the symmetry-breaking bifurcation of the flow. As the channel Reynolds number continues to increase, the length of the short separation zone remains constant, while the length of the long separation zone increases. In addition, some quantitative investigations have been carried out on other types of bifurcated flow under low Reynolds numbers, such as laminar isothermal planar opposed-jet flow [14], parallel wakes, and non-parallel wakes [15].

Different from the macro-scale situation, the laminar impinging slot jet at low Reynolds number under small-scale occasions exhibits more novel unsteady flow and heat transfer behaviors. Especially when the jet Reynolds number exceeds the critical Reynolds number of the steady flow, as the Reynolds number increases, the jet exhibits various forms of unstable flapping motion due to the bifurcation of the flow. Cho [16] conducted a direct numerical simulation of a laminar slot jet at low Reynolds numbers impacting on a flat plate in a two-dimensional confined space with a large height ratio (H/W=10). His numerical results illustrated that when the Reynolds number is 120, the flow field is steady and symmetrical about the jet axis. However, when the Reynolds number increases to between 130 and 150, the flow bifurcates into an impulsive intermittent state, and when the Reynolds number increases to 160, a continuous sinusoidal flapping state appears. Recently, the unsteady flow characteristics and surface Nusselt numbers of a confined, milliscale, laminar impinging slot jet were experimentally studied by Lee et al. [17]. It is found that according to different Reynolds numbers and height ratios, the unsteady flow pattern of the jet can be divided into three types, including a flow fluctuations motion, an intermittent flapping motion of the jet column, and a continuous sinusoidal oscillation state. In addition, the flow fluctuations motion and the intermittent flapping motion affect the local maximum in the Nusselt number distribution. Furthermore, Lee et al. [18] experimentally investigated the heat transfer characteristics when the plate surface is isothermal. Compared with the previous results [17], it is shown that near the stagnation zone, the heat transfer capacity of the plate surface with constant temperature is higher than that of constant surface heat flux, indicating that the laminar boundary layer under the impingement of the laminar jet is very sensitive to the thermal boundary conditions.

A few recent investigations have further analyzed the flow bifurcation, flow field, and thermal field of the laminar impinging slot jet at low Reynolds number in a two-dimensional confined space through linear stability analysis or global stability analysis. Chatterjee et al. [19] performed a numerical study on the flow and heat transport characteristics of the laminar impinging slot jet in a two-dimensional confined space with a large height ratio of 10, and the Reynolds number varied from 90 to 150. Their results indicate that within the range of Reynolds number, $\Delta Re\approx 40$, the steady flow field exhibits hysteresis, and the steady flow bifurcates to unstable solutions. Furthermore, the results of linear stability analysis show that the antisymmetric characteristics of the perturbed Nusslet number and the temperature mode are similar to the unstable velocity mode on the upper branch. Similarly, Chatterjee et al. [20] also employed linear stability analysis to investigate the planar non-Newtonian confined laminar slot impinging jet with a height ratio of 8. Meliga et al. [21] carried out a global stability analysis of a laminar slot jet impinging a flat plate in a two-dimensional confined space with a small height ratio of 2 and found that the flow is unstable to three-dimensional symmetric and antisymmetric steady global modes.

A review of the literature has revealed that most investigations on the laminar impinging jet at low Reynolds number in small-scale geometric configuration mainly focus on the flow characteristics in the channel and heat transfer features of the flat plate surface during the unsteady flapping motion stage of the jet. However, there is a lack of detailed discussion on the driving mechanism of different patterns of unsteady flapping motion of the jet. There is also no investigation to analyze the unsteady flow and heat transfer characteristics in different periods of an intermittent flapping motion of the jet. Furthermore, the dynamic mode decomposition (DMD) is a data-driven method that can extract dynamic information from flow fields obtained from unsteady experimental measurements or numerical simulations. Therefore, the dynamic mode decomposition we carried out has the main goal of intensively investigating the unsteady flow characteristics of different unsteady patterns due to the bifurcation. The DMD method is described in detail in Section 3.4.

As such, in the present study, a numerical investigation is carried out concerning the laminar slot impinging jet at low Reynolds numbers of 120, 150, 200, and with a large height ratio of 10 in a confined channel. The investigations at three different Reynolds numbers are used to understand the flow and heat transfer characteristics of steady flow, and different patterns of unsteadiness due to bifurcation. Based on some time snapshots of the flow field, the dynamic characteristics and driving mechanism of the intermittent flapping motion of the jet column and the continuous sinusoidal flapping state are explained. The flow field of the intermittent flapping motion of the jet is analyzed in detail, in order to present the flow and heat transfer

characteristics in different periods, including the initial stage of the formation of unsteady flapping motion, the unsteady flapping motion stage, and unsteady flapping motion returning to the steady stage. Further, the dynamic mode decomposition method is implemented to accurately extract flow modes with characteristic frequencies of the intermittent flapping motion and continuous sinusoidal flapping state, and the dynamic characteristics of the unsteady flow are illustrated.

2. Problem Description

A two-dimensional jet enters a channel with a height of H and a length of L from a nozzle of width W, and then impacts the surface of the flat plate and flows out from the outlets on both sides of the channel. The computational domain and coordinate system for the configuration are shown in Fig. 1, where all geometric parameters and position coordinates are presented in dimensionless form scaled with the nozzle width of W. The geometric parameters of the channel are fixed; the height ratio is $e=H/W=10$ and the length ratio is $L/W=140$. The inlet boundary of the jet is set at the position $y=-20$. The channel length L can satisfy the full development of the flow at the exit of the channel for the jet Reynolds number range in the investigation, which is confirmed by comparing the velocity profiles at different positions near the channel outlets.

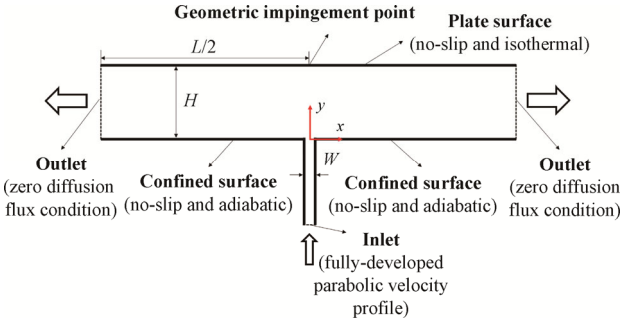

Fig. 1 Schematic diagram of a two-dimensional confined impinging jet

3. Methodology

3.1 Governing equations and boundary conditions

In the present study, the flow is assumed to a two-dimensional, unsteady, and laminar. Since the research object is a slot impinging jet, which has a longer length in the span direction, it can be assumed to be two-dimensional. In addition, the unsteady flow phenomenon of the laminar slot jet impacting the plate surface at low Reynolds numbers has been observed in the experiment [18]. Chatterjee et al. [19] concluded that the flow unsteadiness is a consequence of the bifurcation of the steady flow to an unstable branch of steady solutions through the linear stability analysis method. In the Cartesian coordinate system, the dimensionless governing equations including continuity, momentum, and energy equations are written in vector form as follows:

$$\nabla \cdot \boldsymbol{u} = 0 \tag{1}$$

$$\frac{\partial \boldsymbol{u}}{\partial t} + \boldsymbol{u} \cdot \nabla \boldsymbol{u} = -\nabla p + \frac{1}{Re} \nabla^2 \boldsymbol{u} \tag{2}$$

$$\frac{\partial \theta}{\partial t} + \boldsymbol{u} \cdot \nabla \theta = \frac{1}{Re \cdot Pr} \nabla^2 \theta \tag{3}$$

The dimensionless variables in the governing equations are defined as follows:

$$\boldsymbol{u} = \frac{\hat{\boldsymbol{u}}}{U}, t = \frac{U\hat{t}}{W}, p = \frac{\hat{p}}{\rho U^2}, \theta = \frac{\hat{T} - T_0}{T_w - T_0} \tag{4}$$

where ρ, U, T_0, and T_w are the density, mean inlet velocity of the jet, the inlet temperature of the jet, and temperature of the impinging surface, respectively. $\boldsymbol{u}$, t, p, θ represent the dimensionless velocity vector, time, pressure, and temperature, respectively. The variables with superscript "^" in Eq. (4) represent the corresponding dimensional variables. Then, the dimensionless parameters including Reynolds number and Prandtl number are defined as $Re=\rho UW/\mu$ and $Pr=c_p\mu/k$, where μ, c_p, and k are respectively dynamic viscosity, specific heat at constant pressure, and thermal conductivity. In present study, the Prandtl number is taken as 0.72, and the corresponding cooling fluid is air. The dimensionless parameter that characterizing the heat transfer capacity of the plate surface is taken as the Nusselt number. The local instantaneous Nusselt number Nu and local time-averaged Nusselt number $\overline{Nu}$ are defined as follows:

$$Nu = \frac{hW}{k} = \left.\frac{\partial \theta}{\partial y}\right|_{y=10} \tag{5}$$

$$\overline{Nu} = \frac{1}{t_2 - t_1} \int_{t_1}^{t_2} Nu \mathrm{d}t \tag{6}$$

where h is the local instantaneous convective heat transfer coefficient of the flat surface.

At the nozzle inlet, a fully-developed parabolic velocity profile is specified based on Reynolds number Re and slot width W, and the inflow temperature is set to $\theta=0$. Both the slot and confined surface are adiabatic. At the hot impingement surface, a constant temperature of $\theta=1$ is applied. All walls are employed with no-slip boundary conditions. The zero diffusion flux condition provided at the outlet plane means that the velocity and temperature gradients in the direction normal to the outlet plane are zero, which is especially suitable for fully-developed channel flow. The reference pressure of the outlet is set to zero.

3.2 Numerical methodology

The solver ANSYS Fluent 17.0 [22] is used for all the computations in present study. It solves iteratively continuity, two-dimensional momentum, and energy equations on block-structured quadrilateral meshes based on a finite volume method. The laminar flow model [22] in ANSYS Fluent 17.0 is adopted in present study by directly solving the governing equations. The coupling between the velocity and pressure is carried out by the SIMPLE algorithm. The SIMPLE algorithm [22] uses a relationship between velocity and pressure corrections to make mass conservation and to obtain the pressure field. For the time discretization method, a second order implicit method is used. The diffusive and convective terms are discretized using the second-order central-difference formulation and QUICK scheme respectively [8]. For structural grids aligned with the flow direction, the QUICK scheme [22] can produce more accurate calculation results than the second-order upwind scheme. The QUICK scheme is often used for quadrilateral (hexahedral in three-dimensional) meshes, which is very suitable for the present study. The convergence at each time step is declared when the residuals of the continuity, momentum, and energy equations are all less than 10^{-6}. The CFL number is related to the stability of numerical calculation. The dimensionless time steps of Re=150 and 200 are respectively set to 0.0546 and 0.0582, which can make sure that the CFL numbers are much less than one [19].

3.3 Numerical grid resolution

A quadrilateral mesh of the computational domain is generated in the software ANSYS ICEM 17.0. Fig. 2(a) shows the details of the grid in the present study. In order to accurately capture the flow structures around the jet, the grid nodes arranged are denser in the middle of the channel. In addition, the grid nodes in areas with the large gradient of flow and thermal parameters are refined, and the normal grid ratios are 1.10, including near-wall surfaces, jet inlet and channel outlet. The grid transitions smoothly in the computational domain.

In order to ensure the accuracy and efficiency of numerical calculation at the same time, a different set of grid nodes 90 670, 110 680, 140 129, 150 700, and 177 380 have been tested for the grid independence study. Fig. 2(b) presents the comparison of the local time-averaged Nusselt number distribution along the plate surface with a different set of grid sizes. The maximum relative error between the local time-averaged Nusselt numbers of grid nodes 150 700 and 177 380 along the plate surface is less than 0.1%. Therefore, the results from the set of the grid with 150 700 nodes are considered grid-independent and selected for the rest of this work.

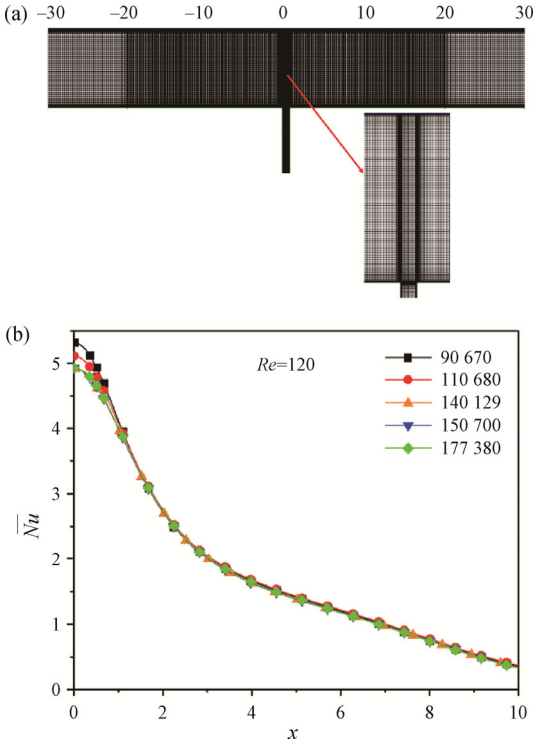

Fig. 2 (a) Details of computation grid and (b) grid independence study

3.4 Dynamic mode decomposition

The dynamic mode decomposition is a data-driven method that can extract dynamic information from flow fields obtained from unsteady experimental measurements or numerical simulations, which was proposed by Schmid [23]. For a series of snapshots, DMD can extract spatial modes (DMD modes), which represent the flow structures, associated with a given temporal frequency. Therefore, DMD can be used to analyze the dominant characteristics of the complex unsteady flows or to establish a low-dimensional flow field dynamic model.

At present, the DMD method has been employed in various flow geometry configurations, including jets [24–26], cavity flow [27, 28], boundary layers [29–32], and wakes [33–36]. Rowley et al. [37] applied DMD to analyze the nonlinear flow of a jet in crossflow and compared the frequency obtained by the direct numerical simulation (DNS), the linearized Navier-Stokes equations, and proper orthogonal decomposition (POD). Their results show that the frequency gained by DMD is the same as the results of DNS, while the frequency obtained by other methods is far from the results of DNS. Iyer et al. [38] carried out DNS of the low-speed transverse jets to study the characteristics of the shear layer, and applied DMD to extract dominant flow structures, explaining the mechanism of shear layer instability. Seena et al. [39] numerically investigated the self-sustained oscillations in

the cavity due to the unsteady separation of the incoming boundary layer and extracted the DMD mode through the DMD method, which corresponds to the coherent structures produced by the self-sustained oscillations.

The DMD method is briefly introduced as follows. At each timestamp, the flow field data such as velocity collected at a fixed time interval Δt is represented as a snapshot, which is arranged as a column of the matrix. Assume that $\boldsymbol{x}_i$ is the snapshot at timestamp i. The number of nodes used to collect data in each snapshot is equal to m, and the total number of snapshots used to record flow field data is equal to n. Then, the snapshot sequence of timestamps from 1 to n can be written as two matrices as follows:

$$\boldsymbol{X}=\left[\boldsymbol{x}_1,\boldsymbol{x}_2,\boldsymbol{x}_3,\ldots,\boldsymbol{x}_{n-1}\right],\boldsymbol{X}'=\left[\boldsymbol{x}_2,\boldsymbol{x}_3,\boldsymbol{x}_4,\ldots,\boldsymbol{x}_n\right] \tag{7}$$

where $\boldsymbol{X},\boldsymbol{X}'\in R^{m\times(n-1)}$. Assume that time consecutive snapshots are connected in time by the best-fit linear operator $\boldsymbol{A}$, as follows:

$$\boldsymbol{x}_{i+1}=\boldsymbol{A}\boldsymbol{x}_i;\quad i\in\left[1,\ldots,n-1\right] \tag{8}$$

where $\boldsymbol{A}$ is the system matrix of the high-dimensional flow field. If the dynamic system is nonlinear, then Eq. (8) represents a linear tangent approximation. Combined with Eq. (7), the snapshot matrices can be expressed as a Krylov sequence:

$$\begin{aligned}\boldsymbol{X}'&=\boldsymbol{A}\boldsymbol{X}=\left[\boldsymbol{A}\boldsymbol{x}_1,\boldsymbol{A}\boldsymbol{x}_2,\boldsymbol{A}\boldsymbol{x}_3,\ldots,\boldsymbol{A}\boldsymbol{x}_{n-1}\right]\\&=\left[\boldsymbol{A}\boldsymbol{x}_1,\boldsymbol{A}^2\boldsymbol{x}_1,\boldsymbol{A}^3\boldsymbol{x}_1,\ldots,\boldsymbol{A}^{n-1}\boldsymbol{x}_1\right]\end{aligned} \tag{9}$$

Take the singular value decomposition (SVD) of $\mathbf{X}$:

$$\boldsymbol{X}=\boldsymbol{U}\boldsymbol{S}\boldsymbol{V}^* \tag{10}$$

where $\boldsymbol{U}\in\mathbb{C}^{n\times r},\boldsymbol{\Sigma}\in\mathbb{C}^{r\times r},\boldsymbol{V}\in\mathbb{C}^{m\times r}$, and the superscript "*" in Eq. (10) denotes the conjugate transpose. r is the rank of the reduced SVD approximation to $\boldsymbol{X}$, which is equal to the number of singular values and $\boldsymbol{\Sigma}$ is the diagonal matrix of the singular values. In order to select the dominant singular values, the following method can be applied:

$$\sigma_i/\sigma_{\max}\le\delta \tag{11}$$

where, σ_i is the i-th singular value, and δ is the selection criterion. Since it is difficult to directly calculate a matrix $\boldsymbol{A}$ when $\boldsymbol{A}$ is a high-dimensional matrix, the reduced-order matrix $\tilde{\boldsymbol{A}}$ is expressed as:

$$\tilde{\boldsymbol{A}}=\boldsymbol{U}^*\boldsymbol{A}\boldsymbol{U}=\boldsymbol{U}^*\boldsymbol{X}'\boldsymbol{V}\boldsymbol{\Sigma}^{-1} \tag{12}$$

Obviously, the reduced matrix $\tilde{\boldsymbol{A}}$ and the full matrix $\boldsymbol{A}$ have the same eigenvalues. Thus, the eigenvalue decomposition of $\tilde{\boldsymbol{A}}$ is computed:

$$\tilde{\boldsymbol{A}}\boldsymbol{W}=\boldsymbol{W}\boldsymbol{\Lambda} \tag{13}$$

where $\boldsymbol{W}$ is the eigenvector matrix, and $\boldsymbol{\Lambda}$ is a diagonal matrix containing the corresponding eigenvalues λ_i. Then, the DMD mode $\boldsymbol{\Phi}$ is obtained:

$$\boldsymbol{\Phi}=\boldsymbol{X}'\boldsymbol{V}\boldsymbol{\Sigma}^{-1}\boldsymbol{W} \tag{14}$$

The growth rate and frequency of DMD mode can be obtained by taking the real part and imaginary part of μ_i. The definition of μ_i is:

$$\mu_i=\lg\left(\lambda_i\right)/\Delta t \tag{15}$$

4. Results

4.1 *Re*=120, a steady laminar regime

Fig. 3 shows the results of the flow and heat transfer in the calculation domain at *Re*=120, which is a steady laminar regime. In order to verify the accuracy of the numerical simulation in the present study, the local time-averaged Nusselt number distribution along the plate surface, and the comparison with the experimental and numerical results in the literature [17, 19] are shown in Fig. 3(a). The numerical results in the present study have good agreement with the experimental results in Ref. [17] and numerical results in the literature [19]. The velocity contour of the steady flow at *Re*=120 is shown in Fig. 3(b). The flow field is axially symmetrical about the jet axis, and the jet perpendicularly impacts the plate

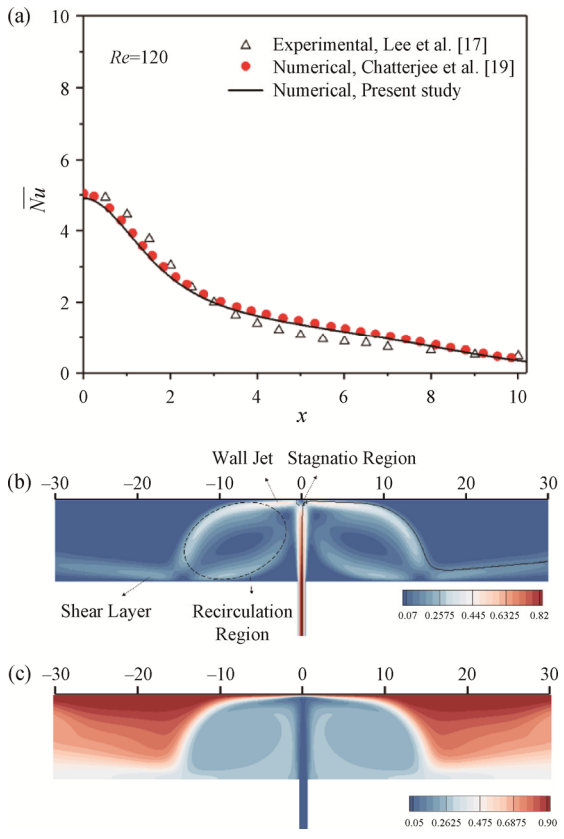

Fig. 3 *Re*=120. Flow and heat transfer under a steady laminar regime. (a) Comparison of the local time-averaged Nusselt number along plate surface with experimental and numerical results. (b) Flow field and (c) temperature distribution in the channel

surface to form a stagnation zone, then turns and accelerates into a wall jet. The more prominent flow feature is that two recirculation zones symmetric about the centerline are generated on both sides of the jet, due to the entrainment of the jet and the restriction of the confined surface. The temperature contour of the steady flow at Re=120 is presented in Fig. 3(c). It is shown that the thickness of the thermal boundary layer is the thinnest in the stagnation zone. As the fluid flows to the wall jet zone, the thickness of the thermal boundary layer gradually increases, resulting in a continuous weakening of the heat transfer capacity along the flow direction.

4.2 *Re*=150, an intermittent flapping motion of the jet column.

Fig. 4(a) plots the transverse velocity component u_x with respect to time at the monitor point (x=0, y=8) on the centerline near the impingement plate surface for Re=150. It is found that the time-varying curve of the transverse velocity component u_x has a distinct intermittent characteristic. From a certain moment, the transverse velocity component u_x fluctuates up and down from zero, and the amplitude gradually increases, which means that the flow transforms from a steady state to an unsteady state. The transverse velocity component u_x does not have a clear changing law and has strong randomness, which reflects the nonlinear characteristics of the intermittent flapping motion. Then, the amplitude of u_x gradually decreases to zero, and the flow field returns to a steady state until the next flapping motion occurs. The fast Fourier transform (FFT) method is used to perform spectrum analysis on the transverse velocity component u_x at the monitor point (x=0, y=8) from time 0 to time 2140, where the frequency is represented by the dimensionless parameter Strouhal number $St_H=fH/U$, as shown in Fig. 4(b). The transverse velocity component u_x demonstrates a distinct spectral peak at St_H=0.408, which is the flapping frequency of the jet column. In addition, Fig. 4(b) also shows several low-amplitude peak frequencies, clarifying that the unsteady flow field of the intermittent flapping motion is very complicated. The comparison between the flapping frequency obtained in the present study and the results in the literature is given in Table 1. The present study indicates a good prediction of the flapping frequency of the jet column when compared with reference data, which further verifies the accuracy of the numerical simulation in the present study. As mentioned earlier, one of the main purposes of this study is to analyze the flow and heat transfer characteristics in different periods under the intermittent flapping motion, which is unique. The change of transverse velocity component u_x at the monitor point (x=0, y=8) with the time from time 0 to time 710 as presented in Fig. 4(c), and some characteristic moments for analyzing the flow and heat transfer are marked. Here, time 1 and 2 (t1 and t2) correspond to the initial stage of the formation of unsteady flapping motion; t3–t7 correspond to roughly one cycle of the jet column flapping motion, and t8–t9 correspond to the stage when the unsteady flow returns to the steady flow.

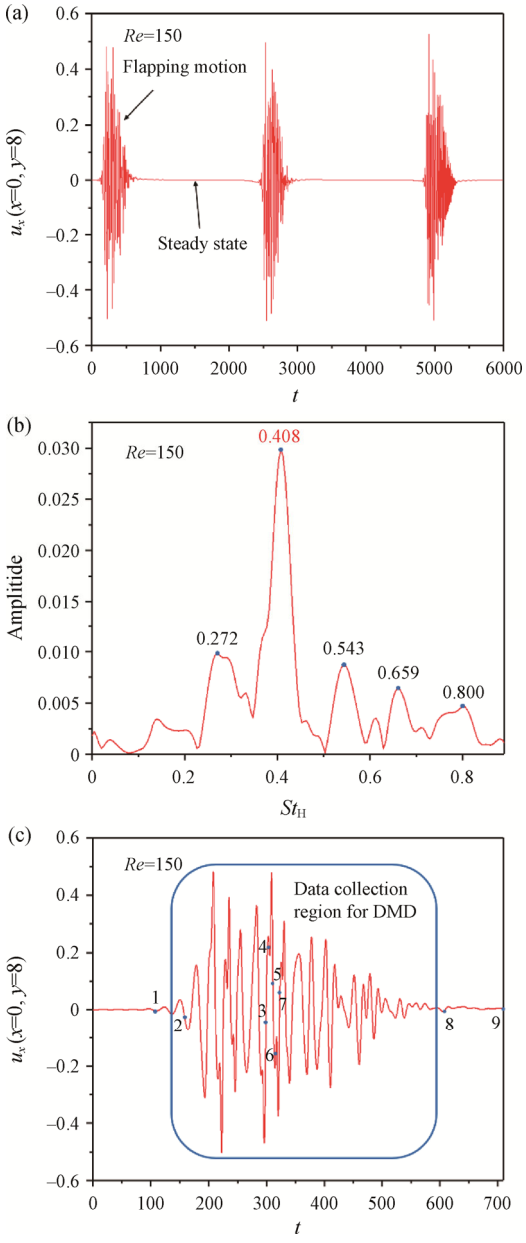

Fig. 4 Re=150 at the monitor point (x=0, y=8). (a) Transverse velocity component u_x plot with respect to time (time 0–6000), (b) spectral analysis of transverse velocity component u_x, and (c) transverse velocity component u_x plot with respect to time (time 0–710), where the characteristic moments and data collection region for DMD are marked.

Table 1 Comparison of flapping frequency

Investigations	Methods	Reynolds number *Re*	Height ratio *H*/*W*	Flapping frequency St_H
Cho [16]	Numerical	150	10	0.470
Brouilliot [40]	Experimental	150	8	0.464
Chatterjee et al. [19]	Numerical	150	10	0.400
Present study	Numerical	150	10	0.408

The pressure distribution in the channel at t1 and t2 are presented in Fig. 5(a) and 5(b), respectively. At t1, the pressure distribution is symmetrical about the centerline, and the flow field is still steady. However, a low-pressure region occurs near the nozzle exit on the right side of the jet column, which indicates that the flow field has begun to enter the unsteady stage. Then, the pressure disturbance gradually enlarges and spreads to the surrounding flow field, while the amplitude of the jet column flapping motion along the plate surface gradually increases. These are observed in subsequent flow field snapshots and are not shown here for brevity. Fig. 5(c) shows the local instantaneous Nusselt number distribution along the plate surface at t1 and t2. It can be found that the local instantaneous Nusselt number distribution is symmetrical about x=0 at t1. At t2, the stagnation point shifts slightly to the left of x=0, and the overall distribution of the local instantaneous Nusselt number begins to become asymmetric about x=0. Therefore, at the initial stage of the formation of unsteady flapping motion for Re=150, the heat transfer characteristics of the plate surface are sensitive to the slight changes in the flow field.

In order to clarify the unsteady flow characteristics when the jet column is in the flapping motion stage, the vorticity contours ($\omega_z = \dfrac{\hat{\omega}_z W}{U}$, where $\hat{\omega}_z$ is z component of vorticity vector) at t3–t7 are assessed in Fig. 6, which roughly correspond to one cycle of the flapping motion of the jet column. At the same time, streamlines are released inside the jet column, the boundary of the primary recirculation zones, and the center of the primary recirculation zones. For ease of analysis, the vortices in the primary recirculation zones are denoted as R1 and R2, and the vortices in the secondary recirculation zones near the confined surface are denoted as R3 and R4, respectively. As shown in Fig. 6(a), at t3, the vortex 1 and vortex 2 formed by the jet shearing and entraining the surrounding fluid can be clearly identified. Vortex 1 has moved to the vicinity of the plate surface and interfered with the boundary layer, while vortex 2 continues to move towards the plate surface. The asymmetrical movement of vortex 1 and vortex 2 causes the jet column to buckle and deflect. The wall jet is separated from the plate surface due to the adverse pressure gradient, and the fluid flows into the

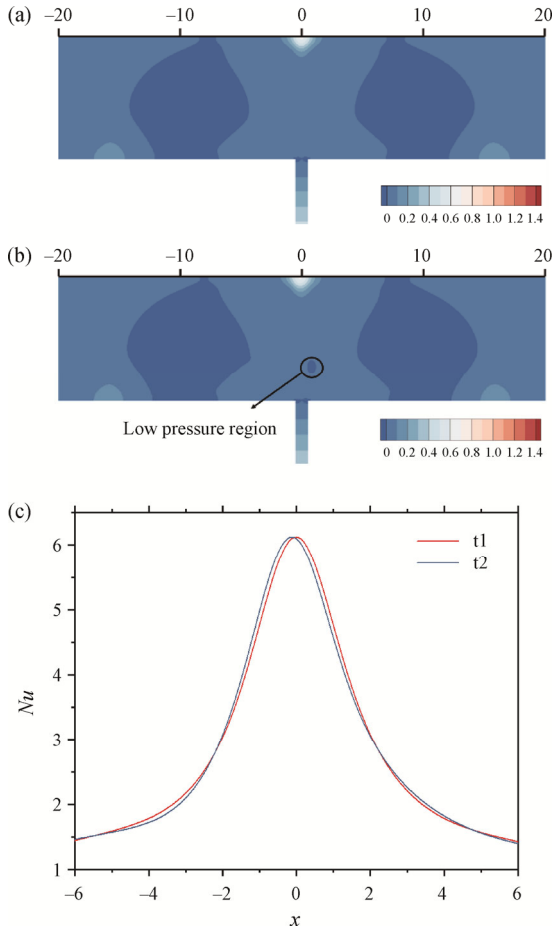

Fig. 5 *Re*=150. The pressure distribution in the channel and the Nusselt number distribution on the plate surface during the initial stage of the formation of unsteady flapping motion: (a) the pressure contour at t1, (b) the pressure contour at t2, and (c) the local instantaneous Nusselt number distribution along the plate surface at t1 and t2

primary recirculation zones or flows to the channel outlet. In addition, a pair of vortices are formed near the plate surface, with similar strength and opposite rotation directions, which is called vortex dipole that has been observed in experiments [10]. According to Fig. 6(b)–(e), vortex 1 moves to the left along the plate surface, and when vortex 1 moves away from the plate surface, it interferes with the boundary layer to form the vortex dipole 1–3, and then vortex 1 and vortex 3 gradually

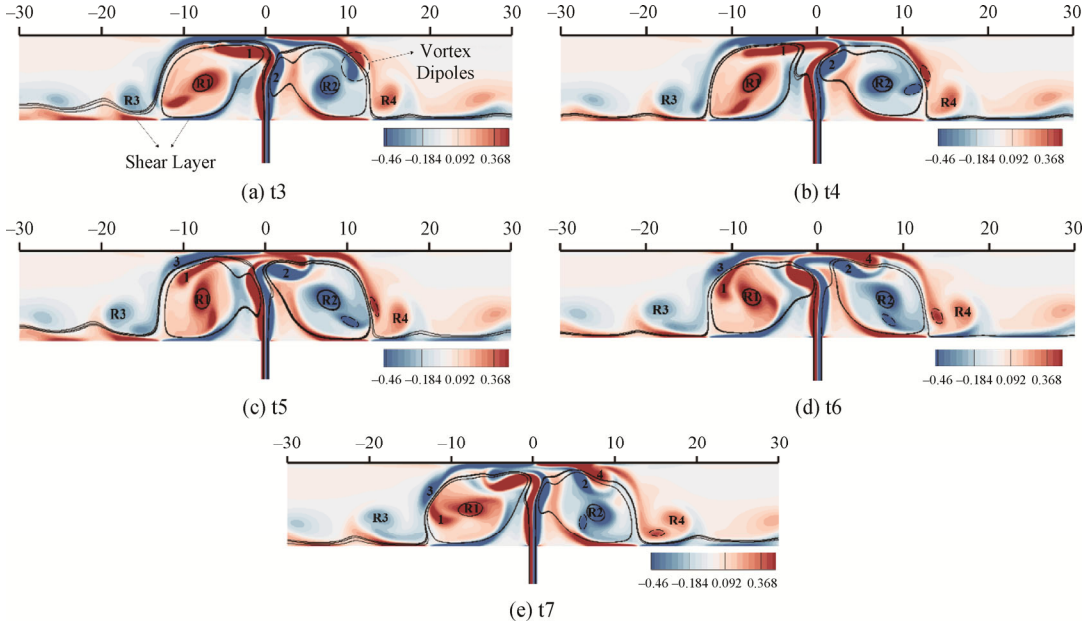

Fig. 6 *Re*=150. Time sequence of vorticity contours during the unsteady flapping motion of the jet column

dissipate. Finally, the high vorticity zones 1 and 3 are respectively entrained into the R1 and R3. The flow inside the right side of the channel is similar to the left side, and the dominant flow characteristic in the channel is a high-amplitude periodic lateral "flapping" jet motion. In order to further illustrate the driving mechanism of the periodic flapping motion of the jet column under the geometric configuration of small nozzle size and a large height ratio, the focus is on the streamlines at different positions as shown in Fig. 6. It is shown that the position and shape of the vortex R1 and vortex R2 are different, and with the rotation of the two vortices, the shear layers formed between the primary recirculation zones and the confined surface produce flow separation. The asymmetric interference between the separated flow and the jet leads to the formation of asymmetric vortices on both sides of the jet column, which causes the jet column to deflect, buckle and flap against the target wall. It is inferred that the flapping motion of the jet column depends on the complex nonlinear coupling between the jet and the asymmetric primary recirculation zones.

Fig. 7 presents the local instantaneous Nusselt number of the plate surface in the range of $x \geq 0$ at t3–t7, since the flow field and heat transfer features on both sides of the centerline are similar. In addition, in order to obtain the heat transfer characteristics of the stagnation zone, the local instantaneous Nusselt number distribution in the range of $x=-5$ to 5 is also given in Fig. 6. The single peak of Nusselt number in the stagnation zone cannot be clearly distinguished but is characterized by broad peaks. This heat transfer characteristic of the stagnation zone can be explained as the jet does not impinge vertically on the plate surface, but flaps greatly along the plate surface,

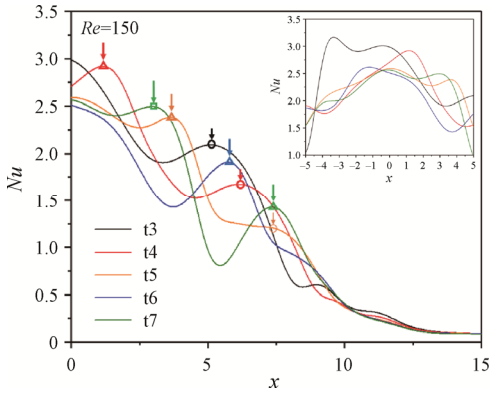

Fig. 7 *Re*=150. The local instantaneous Nusselt number distribution on the plate surface at different times during the unsteady flapping motion of the jet column, where the triangle, circle, and square symbols represent the Nusselt number peaks produced by the interference between different vortices and the boundary layer of the plate surface

resulting in a larger range of stagnation zone. It is worth noting that at different times, there are multiple Nusselt number peaks along the plate surface within the range of $x \geq 0$, and as time increases, the position of the Nusselt number peak gradually moves to the positive direction of the x-axis and the peak value also declines. Combining Fig. 7 and Fig. 6, it can be found that at t4, a Nusselt number peak appears at $x=1.15$, which is due to the thinning of the boundary layer by the vortex 2 moving to the target wall. With the increase of time, vortex 2 gradually moves to the right along the plate surface, with the Nusselt number peak position (triangle symbol in Fig. 7) moving to the right. In this process, the vortex intensity weakens and the interference between vortex 2

and the boundary layer of the plate surface gradually decreases, so the corresponding Nusselt number peak value decreases.

In order to investigate the flow characteristics of the unsteady flapping motion returning to the steady stage, the vorticity contours inside the channel at t8 and t9 are shown in Fig. 8(a) and 8(b), respectively. At t8, the vortex R1 and vortex R2 in the primary recirculation zones have similar vortex intensity, opposite rotation directions, and symmetric about the centerline, which suppresses the flapping motion of the jet column. Compared with Fig. 6, the scope of the secondary recirculation zones is enlarged and the shape is more regular. Since the jet stops flapping, the influence on the flow field outside the primary recirculation zones is reduced, and the secondary recirculation zones can gradually establish a steady flow. It is worth noting that at t8, the separation flow near the confined surface is not symmetric about the centerline, and the flow has not reached a steady state. However, at t9, the flow field is symmetrical with respect to the centerline and does not change with time, indicating that the flow has reached a steady state. In addition, compared with the vorticity distribution at t8, the vortex intensity at the primary recirculation zones at t9 decreases slightly. From the above, it can be speculated that the vortex R1 and vortex R2 in the primary recirculation zones are symmetrical about the centerline, rotate in opposite directions, and have similar vortex intensity, which are necessary conditions for suppressing the flapping motion of the jet column. At the same time, the vorticity dissipation in the primary recirculation zones promotes the flow field to reach a steady state.

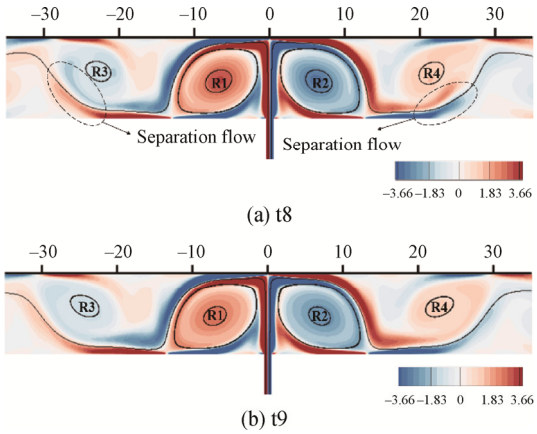

Fig. 8 *Re*=150. The vorticity distribution inside the channel when the unsteady flapping motion is restored to the steady state: (a) vorticity contour at t8, and (b) vorticity contour at t9

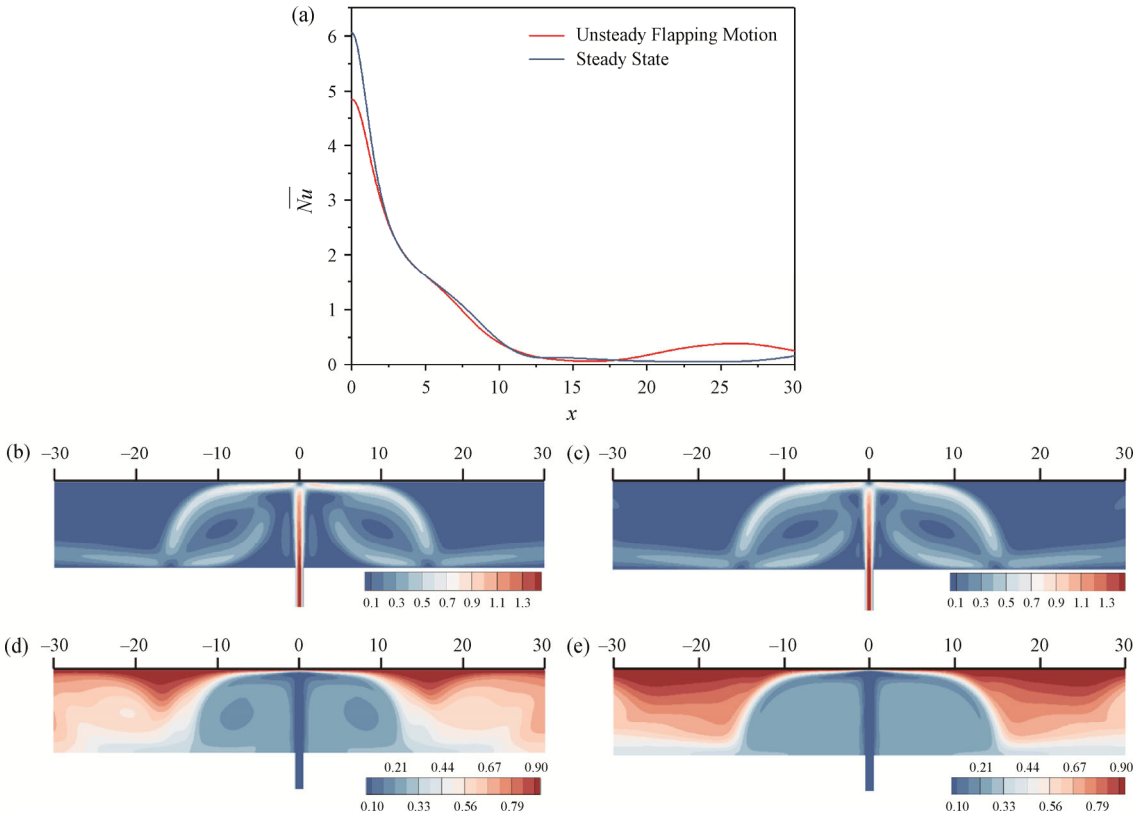

Fig. 9 *Re*=150. (a) Local time-averaged Nusselt number distribution along the plate surface ($x \geq 0$) in the unsteady state and steady state. Time-averaged velocity distribution in the channel during the (b) unsteady state and (c) steady state. Time-averaged temperature distribution in the channel during the (d) unsteady state and (e) steady state

In order to obtain the time-averaged heat transfer characteristics of the target surface in the unsteady state and the steady state stage, Fig. 9(a) shows the local time-averaged Nusselt number of the plate surface during the unsteady state and steady state respectively. The value of the Nusselt number peak at the geometric stagnation point in the steady stage is significantly greater than that in the unsteady stage, which is caused by the flapping motion of the jet to weaken the impact on the center of the plate surface. However, in the range of approximately x=18 to 30, the local time-averaged Nusselt number of plate surface under the unsteady state is higher than that under the steady state. The time-averaged velocity distribution of the unsteady flow and steady flow are respectively presented in Fig. 9(b) and 9(c). It is shown that compared with the steady flow, the primary recirculation zones obtained by the time-averaged velocity field of the unsteady flow are offset to the outside of the jet, which is closely related to the flapping motion of the jet column. The time-averaged temperature field in the unsteady stage and steady stage are respectively shown in Fig. 9(d) and 9(e). The time-averaged results show that in the range of x=18 to 30, the thermal boundary layer in the unsteady state is thinner than in the steady state, which corresponds to the distribution of the local time-averaged Nusselt number along the plate surface.

4.3 *Re*=200, a continuous sinusoidal flapping state

When Re=200, the flow bifurcates to a continuous sinusoidal flapping state. The change of transverse velocity component u_x at the monitor point (x=0, y=8) with the time in different periods as presented in Fig. 10(a) and 10(b), respectively. It can be found that the transverse velocity component u_x always maintains a continuous sinusoidal oscillation state. From a moment, the oscillation amplitude gradually increases from the minimum value, and after reaching a maximum value, it gradually decreases to the initial amplitude, forming a large cycle. The FFT method is used to perform spectrum analysis on the transverse velocity component u_x at the monitor point (x=0, y=8) from time 0 to time 1750, as shown in Fig. 10(c). There is a dominant frequency St_H=0.921 with the highest amplitude, and the remaining peak frequencies distributed on the left and right sides are close to the dominant frequency, all of which are related to the continuous sinusoidal flapping motion. In addition, except that the difference between the peak frequency St_H=0.939 and St_H=0.921 is 0.018, the difference between the other two adjacent peak frequencies is 0.017, which corresponds to the change frequency of the transverse velocity component u_x amplitude.

In order to obtain the unsteady flow characteristics of the continuous sinusoidal flapping state at Re=200, the vorticity contours at t1–t5 (Fig. 10(b)) are respectively presented in Fig. 11, which roughly correspond to a flapping cycle of the jet column. At t1, vortex 1 causes the jet column to deflect to the left of x=0, while the velocity fluctuation is transmitted downstream and a separation bubble is generated near the plate surface on the left of the primary recirculation zone. From Fig. 11(b)

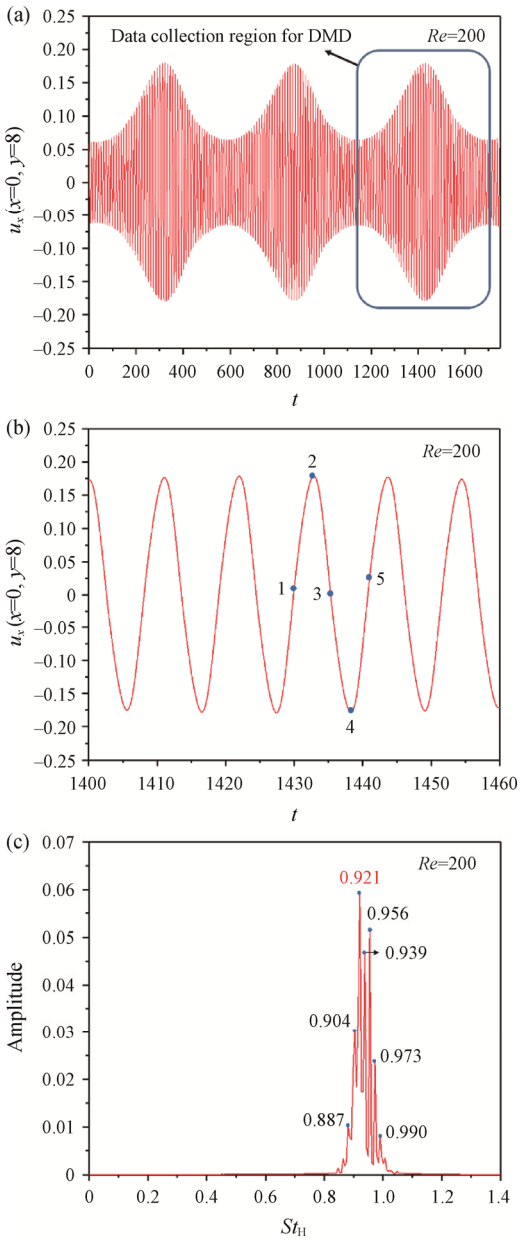

Fig. 10 Re=200 at the monitor point (x=0, y=8). (a) Transverse velocity component u_x plot with respect to time (time 0–1750), where the data collection region for DMD are marked. (b) Transverse velocity component u_x plot with respect to time (time 1400–1460), where the characteristic moments are marked. (c) Spectral analysis of transverse velocity component u_x.

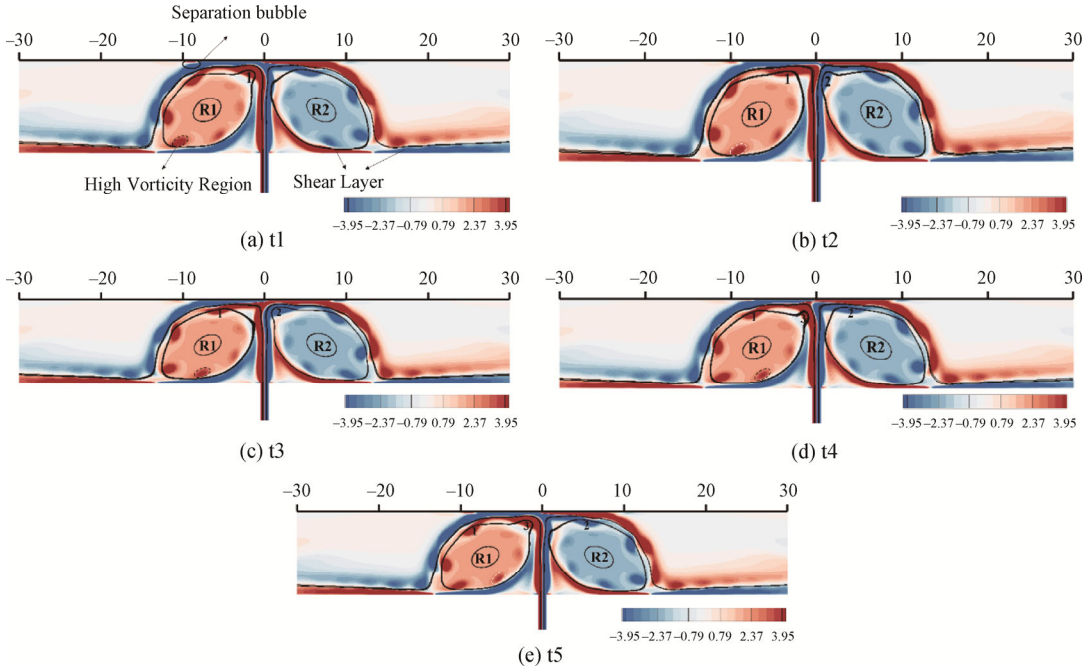

Fig. 11 Time sequence of vorticity contours for *Re*=200

to 11(e), it can be found that as time increases, vortex 1 gradually moves to the left along the plate surface, and vortex 2 is generated near the plate surface on the right of the jet column, resulting in the deflection of the jet column to the right. After that, vortex 1 and vortex 2 continue to move along the boundary of the primary recirculation zones and gradually dissipate into high vorticity zones. Then, vortex 3 is formed on the left side of the jet column, causing the deflection of the jet column to the left again. It can be seen that the vortices formed alternately on the left and right sides of the jet column cause the jet to flap periodically. However, the strength of the vortices at the center of the primary recirculation zone on both sides of the jet column is similar, and the shape of the vortices does not change during the flapping motion and is always symmetrical about the centerline. In addition, the high vorticity zones have been moving along the boundary of the primary recirculation zones, and have not been involved in the vortices at the center of the primary recirculation zones, which is different from the flapping motion stage of the jet column at *Re*=150. In summary, the velocity disturbance generated by the flapping motion of the jet column is mainly in the form of high vorticity zone and propagates upstream asymmetrically along the boundary of the primary recirculation zones, thus forming a feedback loop that maintains the continuous sinusoidal flapping motion.

In order to analyze the unsteady heat transfer characteristics under the continuous sinusoidal flapping state, Fig. 12 presents the local instantaneous Nusselt

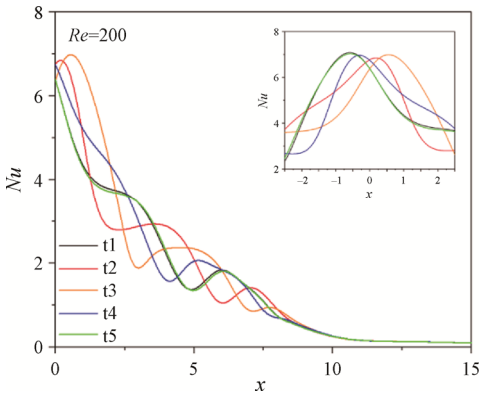

Fig. 12 *Re*=200. The local instantaneous Nusselt number distribution on the plate surface at different times

number distribution along the plate surface ($x \geq 0$) from t1 to t5. When *Re*=200, there is an obvious Nusselt number peak in the stagnation area at each moment, which is different from the Nusselt number distribution at *Re*=150. In addition to the stagnation zone, there are other Nusselt number peaks along the plate surface, and as time increases, the positions of these Nusselt number peaks gradually move to the right with the values of Nusselt number peaks decreasing, which mainly depends on the interference between the shedding vortex and the boundary layer.

4.4 Dynamic mode decomposition results: *Re*=150 and *Re*=200

The dynamics of the unsteady flow field in the channel at *Re*=150 and *Re*=200 are investigated through

the modal decomposition technique, namely dynamic mode decomposition in this section. The snapshot data collection regions for DMD analysis at Re=150 and Re=200 are shown in Fig. 4(c) and Fig. 10(a), respectively.

Based on the unsteady results of Re=150, a total of 400 snapshots of the flow field are extracted at the same time interval. The velocity field ($\hat{u}_x$, $\hat{u}_y$ and $\hat{u}=\sqrt{\hat{u}_x^2+\hat{u}_y^2}$) is analyzed using the DMD method, and Fig. 13 presents the frequency-energy distribution correspondingly. It can be found that there are frequencies corresponding to high local energy values, where St_H=0.422 is the flapping frequency.

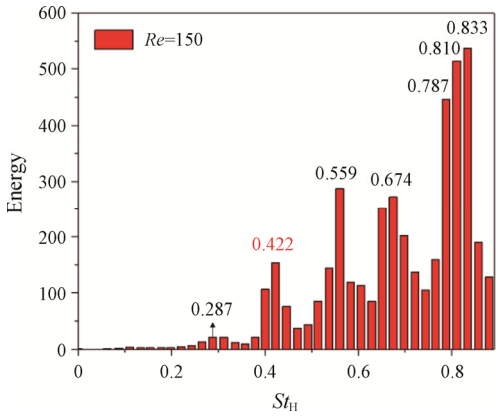

Fig. 13 DMD spectrum obtained from the velocity field for Re=150

Fig. 14 presents the velocity ($\hat{u}$) DMD modes corresponding to the frequencies of high local energy at a Reynolds number of 150. From Fig. 14(a), it can be found that the velocity mode corresponding to the frequency St_H=0.422 is distributed antisymmetrically with respect to the centerline, and there are three pairs of velocity fluctuation structures with opposite signs in the middle of the channel. In addition, along the flow direction in the middle of the channel, the signs of the velocity fluctuation structures also change alternately between positive and negative. This velocity mode reflects the characteristics of the periodic lateral flapping of the jet, which is the flapping mode. The velocity modes in Fig. 14(b), 14(c), and 14(d) correspond to higher frequencies (St_H=0.559, 0.674, 0.810), and the distribution of velocity fluctuation structures in the channel is more complicated. These higher frequency modes mainly describe the flow details inside the jet and the recirculation zone.

At a Reynolds number of 200, the frequency-energy distribution obtained from the analysis of the velocity field ($\hat{u}_x$, $\hat{u}_y$ and $\hat{u}=\sqrt{\hat{u}_x^2+\hat{u}_y^2}$) by the DMD method is shown in Fig. 15. The energy amplitude of the mode corresponding to the frequency St_H=0.919 is the highest, and there are several frequencies with high energy amplitude around the frequency St_H=0.919, all of which are related to the flapping motion of the jet. Near the vertical axis, the DMD method also identified a relatively obvious peak frequency St_H=0.018, which is the difference between two adjacent peak frequencies related to the flapping motion. In addition, the frequency St_H=

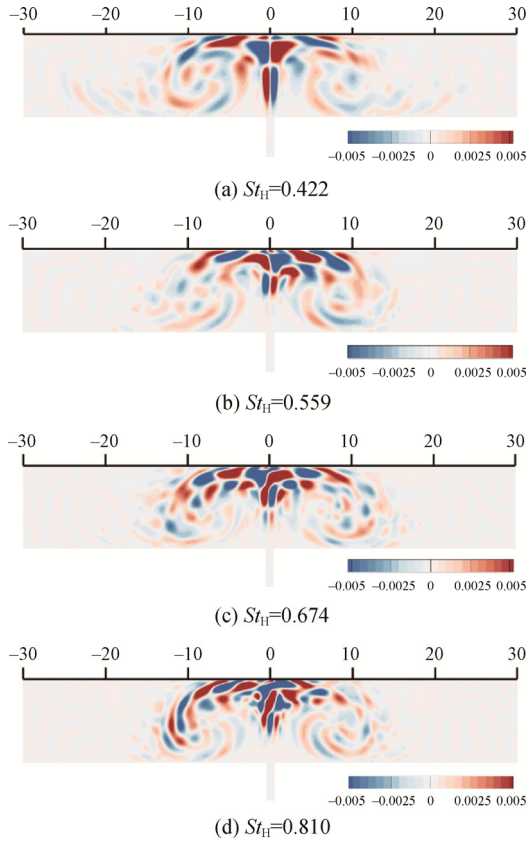

Fig. 14 Re=150. Velocity DMD modes corresponding to different frequencies

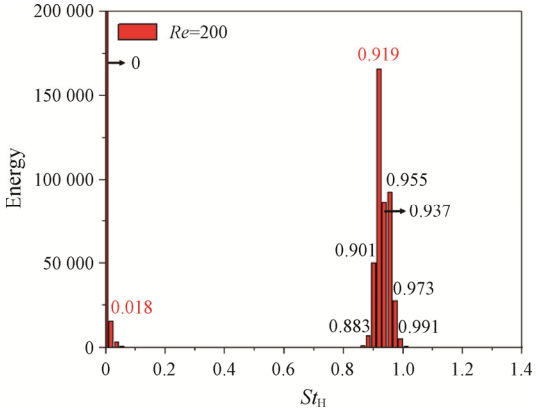

Fig. 15 DMD spectrum obtained from the velocity field for Re=200

0.018 is very similar to the change frequency (St_H=0.017) of the amplitude of transverse velocity component u_x at the monitor point (x=0, y=8).

Fig. 16(a)–(g) respectively present the velocity DMD modes corresponding to the frequencies with high local energy, where St_H=0.883, 0.901, 0.919, 0.937, 0.955, 0.973 and 0.991, which are almost consistent with the peak frequencies obtained by the FFT method. These velocity modes are all antisymmetric about the centerline. In the middle of the channel, there are velocity fluctuation structures of similar size and opposite signs, and the signs of the fluctuating structures along the flow direction also change positively and negatively. The above velocity modes all reflect the lateral flapping motion of the jet. In addition, these flapping modes are slightly different at the boundary of the recirculation zone, which all reflects the transmission of velocity fluctuation along the flow direction and the "jitter" of the boundary of the recirculation zone perpendicular to the flow direction. The frequency difference between two adjacent modes in Fig. 16(a)–(g) is 0.018, so it can be inferred that the velocity mode corresponding to the low frequency St_H=0.018, as shown in Fig. 16(h), is related to the coupling between the flapping modes. It is interesting that the mode corresponding to the frequency St_H=0.018 is axisymmetric about the centerline, and the velocity fluctuation structures are distributed at the boundary of the recirculation zones, which mainly describes the shear flow at the boundary of the recirculation zones.

In order to further explore the dynamic characteristics of the velocity mode corresponding to the frequency St_H= 0.018, the instantaneous velocity field is projected on each of the selected DMD modes, where the corresponding frequencies are St_H=0 and St_H=0.018, and then all the projections are added to generate the reconstructed flow field. Fig. 17 shows the reconstructed velocity field snapshots taken at the same time interval, acquiring one cycle of the lowest frequency (St_H=0.018) period motion. In addition, for convenience of observation, the areas with relatively large flow changes over time are marked in Fig. 17. The flow fields at different times are distributed axisymmetrically about the centerline, which corresponds to the axisymmetric structures of velocity mode with St_H=0.018, as shown in Fig. 16(h). According to Fig. 17(a)–(f), the velocity mode corresponding to frequency St_H=0.018 mainly depicts the periodic changes of the recirculation zone boundary contour and the position of the recirculation zone relative to the jet.

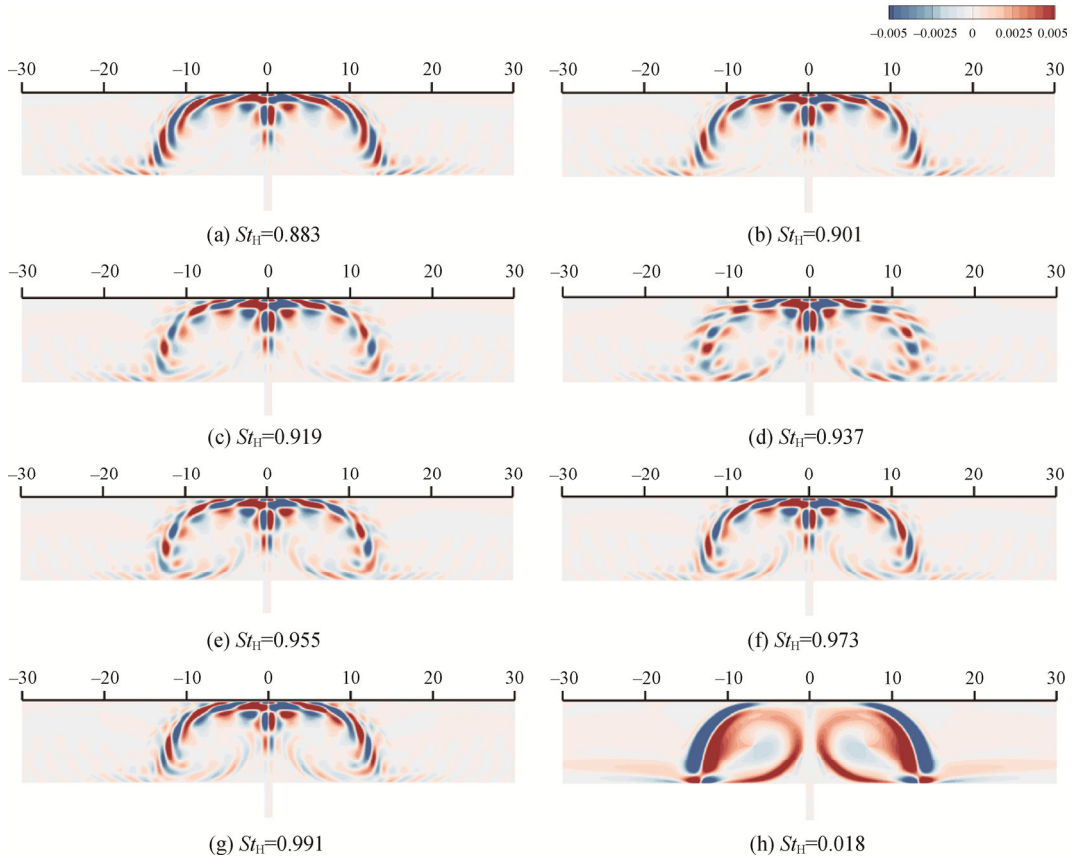

Fig. 16 Re=200. Velocity DMD modes corresponding to different frequencies

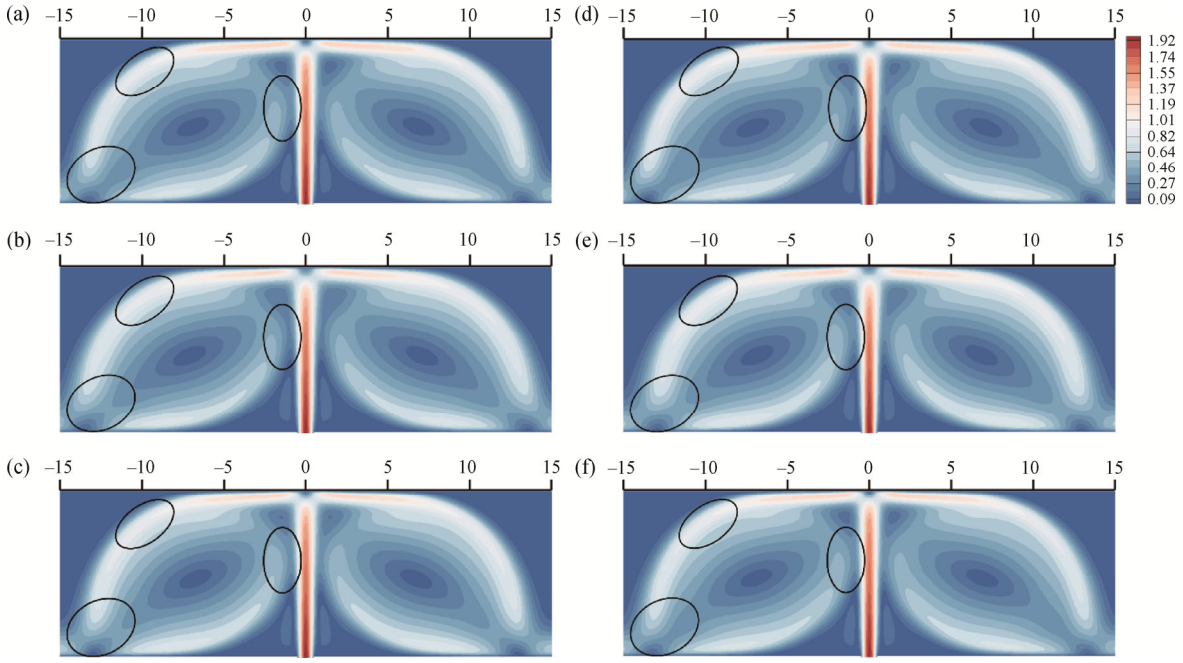

Fig. 17 *Re*=200. The time sequence of the projection of the instantaneous velocity fields for DMD modes (St_H=0 and St_H= 0.018), and the areas with relatively large flow changes over time are marked

5. Conclusions

In the present work, the unsteady flow and heat transfer characteristics of a laminar slot impinging jet at low Reynolds numbers in a two-dimensional confined space are numerically investigated. Numerical investigations are carried out at jet Reynolds numbers of 120, 150 and 200. The height ratio of the channel is 10, and the given temperature of the impact surface is higher than the jet exit temperature. The authenticity of the numerical model is achieved by the grid-independency solution and comparison with the experimental results. Based on some time snapshots of the flow field, the dynamic characteristics, driving mechanism and heat transfer characteristics of the intermittent flapping motion of the jet column (*Re*=150) and the continuous sinusoidal flapping state (*Re*=200) are explained. The DMD method is implemented to accurately extract the flow modes corresponding to different frequencies for *Re*=150 and *Re*=200, and the dynamic characteristics of the unsteady flow are further illustrated. The important conclusions are summarized as follows:

(1) For a Reynolds number of 150, during the flapping motion of the jet column, the shape and position of the vortices in the primary recirculation zones on both sides of the jet column are different. The asymmetric interference between the separation flow of the confined surface and the jet creates asymmetric vortices on both sides of the jet column, causing the jet to deflect, buckle, and flap against the plate surface.

(2) It is speculated that at *Re*=150, the lateral flapping motion of the jet is related to the nonlinear coupling between the jet and the asymmetric recirculation zones. When the flow field recovers from an unsteady state to a steady state, the vortices in the primary recirculation zones on both sides of the jet column are symmetrical about the centerline and have similar vorticity, which inhibits the flapping motion.

(3) For a Reynolds number of 200, the jet is in a continuous sinusoidal flapping state, and the amplitude of the flapping motion also changes periodically. In addition, there are multiple frequencies related to the flapping motion. According to the snapshots of the flow field, the velocity disturbance generated by the flapping motion of the jet propagates upstream along the boundary of the recirculation zones in the form of high vorticity zones, which forms feedback loop that maintains the continuous sinusoidal flapping motion.

(4) For the unsteady heat transfer on the target surface, the local instantaneous Nusselt number distribution in the stagnation zone shows the broad peak at *Re* = 150, while the obvious single peak of the Nusselt number appears in the stagnation zone at *Re*=200.

(5) Regardless of *Re*=150 or 200, other Nusselt number peaks appear outside the stagnation zone during the flapping motion of the jet column, which is different from the steady flow. As time increases, the position of the Nusselt number peaks outside the stagnation zone gradually shifts outward with the values of Nusselt number peaks decreasing, which mainly depends on the

interference between the shedding vortices and the boundary layers.

(6) According to the results of analyzing the unsteady velocity field by the DMD method, the DMD method can accurately capture the characteristic frequencies and the corresponding DMD modes. For a Reynolds number of 150, the DMD mode corresponding to the frequency St_H=0.422 is the flapping mode, which reflects the lateral flapping motion of the jet column along the plate, while the other modes with higher frequencies further describe the flow details inside the jet and the recirculation zones.

(7) When the Reynolds number is 200, the DMD modes corresponding to the frequencies of St_H=0.883, 0.901, 0.919, 0.937, 0.955, 0.973 and 0.991 are all flapping modes. Further, the mode corresponding to the low frequency of St_H=0.018 is related to the coupling between the flapping modes, which depicts the periodic change of the contour and position of the recirculation zones.

Acknowledgment

The authors gratefully acknowledge the support for the research from the National Key R&D Program of China (2018YFB0604404).

References

[1] Zhou J., Wang X., Li J., Influences of effusion hole diameter on impingement/effusion cooling performance at turbine blade leading edge. International Journal of Heat and Mass Transfer, 2019, 134(5): 1101–1118.

[2] Masip Y., Campo A., Nuñez S.M., Experimental analysis of the thermal performance on electronic cooling by a combination of cross-flow and an impinging air jet. Applied Thermal Engineering, 2020, 167: 114779.

[3] Marco P.D., Frigo S., Gabbrielli R., Pecchia S., Mathematical modelling and energy performance assessment of air impingement drying systems for the production of tissue paper. Energy, 2016, 114: 201–213.

[4] Alamir M., Witrant E., Valle G.D., Rouaud O., Josset C., Boillereaux L., Estimation of energy saving thanks to a reduced-model-based approach: example of bread baking by jet impingement. Energy, 2013, 53: 74–82.

[5] Chauhan R., Thakur N.S., Investigation of the thermohydraulic performance of impinging jet solar air heater. Energy, 2014, 68: 255–261.

[6] Webb B.W., Ma C.F., Single-phase liquid jet impingement heat transfer. Advances in Heat Transfer, 1995, 26(08): 105–217.

[7] Shih T., Thamire C., Sung C., Ren A., Literature survey of numerical heat transfer (2000-2009): Part 1. Numerical Heat Transfer, Part A: Applications, 2010, 57(3–4): 159–296.

[8] Chiriac V.O., Ortega A., A numerical study of the unsteady flow and heat transfer in a transitional confined slot jet impinging on an isothermal surface. International Journal of Heat and Mass Transfer, 2002, 45(6): 1237–1248.

[9] Lee H.G., Yoon H.S., Ha M.Y., A numerical investigation on the fluid flow and heat transfer in the confined impinging slot jet in the low Reynolds number region for different channel heights. International Journal of Heat and Mass Transfer, 2008, 51(15–16): 4055–4068.

[10] Varieras D., Brancher P., Giovannini A., Self-sustained oscillations of a confined impinging jet. Flow, Turbulence and Combustion, 2007, 78(1): 1–5.

[11] Uzol O., Camci C., Experimental and computational visualization and frequency measurements of the jet oscillation inside a fluidic oscillator. Journal of Visualization, 2002, 5(3): 263–272.

[12] Lee G.B., Kuo T.Y., Wu W.Y., A novel micromachined flow sensor using periodic flapping motion of a planar jet impinging on a V-shaped plate. Experimental Thermal and Fluid Science, 2002, 26(5): 435–444.

[13] Durst F., Pereira J., Tropea C., The plane Symmetric sudden-expansion flow at low Reynolds numbers. Journal of Fluid Mechanics, 1993, 248: 567–581.

[14] Liu S., Wang B., Wan Z., Ma D., Sun D., Bifurcation analysis of laminar isothermal planar opposed-jet flow. Computers & Fluids, 2016, 140: 72–80.

[15] Chomaz J., Fully nonlinear dynamics of parallel wakes. Journal of Fluid Mechanics, 2003, 495: 57–75.

[16] Cho J.R., Numerical observations of a bifurcating plane impinging jet in a confined channel. Journal of Visualization, 2006, 9(4): 361–362.

[17] Lee D.H., Bae J.R., Park H.J., Lee J.S., Ligrani P., Confined, milliscale unsteady laminar impinging slot jets and surface Nusselt numbers. International Journal of Heat and Mass Transfer, 2011, 54(11–12): 2408–2418.

[18] Lee D.H., Park H.J., Ligrani P., Milliscale confined impinging slot jets: Laminar heat transfer characteristics for an isothermal flat plate. International Journal of Heat and Mass Transfer, 2012, 55(9–10): 2249–2260.

[19] Chatterjee A., Tarbell J., Laminar stability and heat transport in high aspect ratio planar confined impinging flows. International Journal of Heat and Mass Transfer, 2019, 137: 534–544.

[20] Chatterjee A., Fabris D., Planar non-Newtonian confined laminar impinging jets: Hysteresis, linear stability, and periodic flow. Physics of Fluids, 2017, 29(10): 103103.

[21] Meliga P., Chomaz J.M., Global modes in a confined impinging jet: application to heat transfer and control. Theoretical and Computational Fluid Dynamics, 2011, 25: 170–193.

[22] Fluent, Theory Guide. A.N.S.Y.S., Release 17.0, 2016.

[23] Schmid P.J., Sesterhenn J., Dynamic mode decomposition of numerical and experimental data. Journal of Fluid Mechanics, 2010, 656(10): 5–28.

[24] Semeraro O., Bellani G., Lundell F., Analysis of time-resolved PIV measurements of a confined turbulent jet using POD and Koopman modes. Experiments in Fluids, 2012, 53(5): 1203–1220.

[25] Schmid P.J., Li L., Juniper M.P., Pust O., Applications of the dynamic mode decomposition. Theoretical and Computational Fluid Dynamics, 2011, 25(1): 249–259.

[26] Schmid P.J., Violato D., Scarano F., Decomposition of time-resolved tomographic PIV. Experiments in Fluids, 2012, 52(6): 1567–1579.

[27] Basley J., Pastur L.R., Delprat N., Lusseyran F., Space-time aspects of a three-dimensional multi-modulated open cavity flow. Physics of Fluids, 2013, 25(6): 695–719.

[28] Lusseyran F., Gueniat F., Basley J., Douay C.L., Pastur L.R., Faure T.M., Schmid P.J., Flow coherent structures and frequency signature: Application of the dynamic modes decomposition to open cavity flow. Journal of Physics: Conference Series, 2011, 318(4): 042036.

[29] Mizuno Y., Duke D., Atkinson C., Soria J., Investigation of wall-bounded turbulent flow using Dynamic mode decomposition. Journal of Physics: Conference Series, 2011, 318(4): 042040.

[30] Ostoich C.M., Bodony D.J., Geubelle P.H., Interaction of a Mach 2.25 turbulent boundary layer with a fluttering panel using direct numerical simulation. Physics of Fluids, 2013, 25(11): 171–186.

[31] Sayadi T., Schmid P.J., Nichols J.W., Moin P., Reduced-order representation of near-wall structures in the late transitional boundary layer. Journal of Fluid Mechanics, 2014, 748: 278–301.

[32] Lee J.H., Seena A., Lee S.H., Sung H.J., Turbulent boundary layers over rod- and cube-roughened walls. Journal of Turbulence, 2012, 13(40): 1–26.

[33] Tu J., Rowley C., Aram E., Mittal R., Koopman spectral analysis of separated flow over a finite-thickness flat plate with elliptical leading edge. AIAA Aerospace Sciences Meeting Including the New Horizons Forum and Aerospace Exposition, 2011.

[34] Pan C., Yu D., Wang J., Dynamical mode decomposition of Gurney flap wake flow. Theoretical and Applied Mechanics Letters, 2011, 1(1): 012002.

[35] Iungo G.V., Santoni-Ortiz C., Abkar M., Porte-Agel F., Rotea M.A., Leonardi S., Data-driven reduced order model for prediction of wind turbine wakes. Journal of Physics: Conference Series, 2015, 625: 012009.

[36] Dunne R., Mckeon B.J., Dynamic stall on a pitching and surging airfoil. Experiments in Fluids, 2015, 56(8): 157.

[37] Rowley C., Mezic I., Bagheri S., Schlatter P., Spectral analysis of nonlinear flows. Journal of Fluid Mechanics, 2009, 641: 115–127.

[38] Iyer P.S., Mahesh K., A numerical study of shear layer characteristics of low-speed transverse jets. Journal of Fluid Mechanics, 2016, 790: 275–307.

[39] Seena A., Sung H.J., Dynamic mode decomposition of turbulent cavity flows for self-sustained oscillations. International Journal of Heat and Fluid Flow, 2011, 32(6): 1098–1110.

[40] Brouilliot D., Étude experimentale de l'aérothermique et de la dynamique des jets impactants. Ph.D. thesis, Université de Toulouse III, France, 2016.